

ARTICLE OPEN



The precipitation distribution set by eddy fluxes: the case of boreal winter

Changhyun Yoo¹ and Sukeyoung Lee²✉

The latitudinal precipitation distribution shows a secondary peak in midlatitudes and a minimum in the subtropics. This minimum is widely attributed to the descending branch of the Eulerian Hadley cell. This study however shows that the precipitation distribution aligns more closely with the transformed Eulerian mean (TEM) vertical motion. In Northern Hemisphere winter, maximum TEM descent (ascent) and precipitation minimum (maximum) are collocated at $\sim 20^\circ\text{N}$ ($\sim 40^\circ\text{N}$). The subtropical descent is mostly driven by the meridional flux of zonal momentum by large-scale eddies, while the midlatitude ascent is driven by the meridional flux of heat by the eddies. When the poleward eddy momentum flux is sufficiently strong, however, the secondary precipitation peak shifts to 60°N corresponding to the location of the TEM ascent driven by the eddy momentum flux. Moisture supply for the precipitation is aided by evaporation which is enhanced where the TEM descending branch brings down dry air from the upper troposphere/lower stratosphere. This picture is reminiscent of dry air intrusions in synoptic meteorology, suggesting that the descending branch may embody a zonal mean expression of dry air intrusions. Moist air rises following the TEM ascending branch, suggesting that the ascending branch may be interpreted as a zonal mean expression of warm conveyor belts. This study thus offers a large-scale dynamics perspective of the synoptic description of precipitation systems. The findings here also suggest that future changes in the eddy momentum flux, which is poorly understood, could play a pivotal role in determining the future precipitation distribution.

npj Climate and Atmospheric Science (2023)6:24; <https://doi.org/10.1038/s41612-023-00356-9>

INTRODUCTION

Precipitation variability has received considerable attention because precipitation or lack thereof has a large societal impact. An improved understanding of precipitation variability requires a firm grasp of how the climatological mean state arises. It is well established that most of the cold season extratropical precipitation is associated with extratropical cyclones, and the precipitation maximum near 40°N in midlatitudes (bottom panels in Fig. 1) is attributed to extratropical storm activities^{1,2}. Figure 1a shows that the precipitation minimum in the subtropics is not caused by a lack of moisture because the specific humidity is greater in the subtropics than in midlatitudes. Instead, the precipitation minimum is commonly attributed to the climatological high-pressure systems that form under the descending branch of the Hadley cells.

Comparing the precipitation distribution with the Eulerian overturning circulation (Fig. 1b), however, we see that the precipitation minimum peaks at $\sim 20^\circ\text{N}$, while the descending motion, measured by \bar{w}_{500} , is strongest at $\sim 30^\circ\text{N}$. Figure 1c shows that the precipitation minimum instead aligns more closely with the downward mass transport of the residual mean circulation of transformed Eulerian mean (TEM) theory^{3,4}. The TEM is different from the Eulerian overturning circulation in that the former includes a mass transport by the eddies as well as by the zonal mean Eulerian overturning circulation. Moreover, the precipitation maximum at $\sim 40^\circ\text{N}$ roughly coincides with the ascending branch of the residual mean circulation in midlatitudes. These descending and ascending branches form the U-shaped dip (for conciseness “dip” hereafter) in the TEM overturning circulation (Fig. 1c). (Note that unrealistically large TEM streamfunction values below 850 hPa are due to a weak static stability near the surface⁵, which may be remedied by replacing the singular static stability in pressure

coordinate by isentropic static stability near the surface⁶.) Here, we formally define the dip as the region bounded by the maximum downwelling and upwelling (\bar{w}_{500}^*), as indicated by the red vertical lines in Fig. 1c. From this definition, we see that the dip ranges between $\sim 25^\circ\text{N}$ and $\sim 40^\circ\text{N}$. The dip remains robust when the level of the vertical velocity is varied from 500 hPa to 700 hPa.

Using a two-layer model, Robinson⁷ first pointed out that eddy momentum flux (EMF) convergence drives a TEM dip. This is consistent with the “downward control” mechanism in which the distribution of the full EP flux divergence aloft determines the vertical motion at lower levels⁸. The portion of the TEM circulation driven by the EMF contribution (Fig. 2a) exhibits sinking motion centered at $\sim 30^\circ\text{N}$ (Fig. 2d) (calculation described in Materials and Methods), a latitude where the TEM circulation shows sinking motion but is located $\sim 5^\circ$ north of where the sinking motion is strongest. However, the EMF-driven rising motion is centered at $\sim 60^\circ\text{N}$ (Fig. 2d), and it is eddy heat flux (EHF) divergence (Fig. 2b) that drives the ascending branch of the dip at $\sim 40^\circ\text{N}$ (Fig. 2e). The sum of the full eddy flux forcing (Fig. 2c) captures the overall structure of the TEM circulation (compare Fig. 1c and Fig. 2f), although some discrepancies can be observed in the tropics and subtropics where impact of tropical convection cannot be ignored⁹. This analysis indicates that the rather narrow climatological dip, ranging between 25°N and 40°N , arises from the combined effect of the two eddy fluxes. The sinking branch driven by the EMF (30°N) is compensated by the EHF-driven rising motion, resulting in the TEM downward motion between 20°N – 30°N . Similarly, the latitudinal location of the rising branch is also determined by the relative strength of the two eddy fluxes. To the extent that precipitation coincides with the rising/sinking branch of the dip, it follows that the relative strength of the two

¹Ewha Womans University, Seoul, South Korea. ²The Pennsylvania State University, University Park, PA, USA. ✉email: sxl31@psu.edu

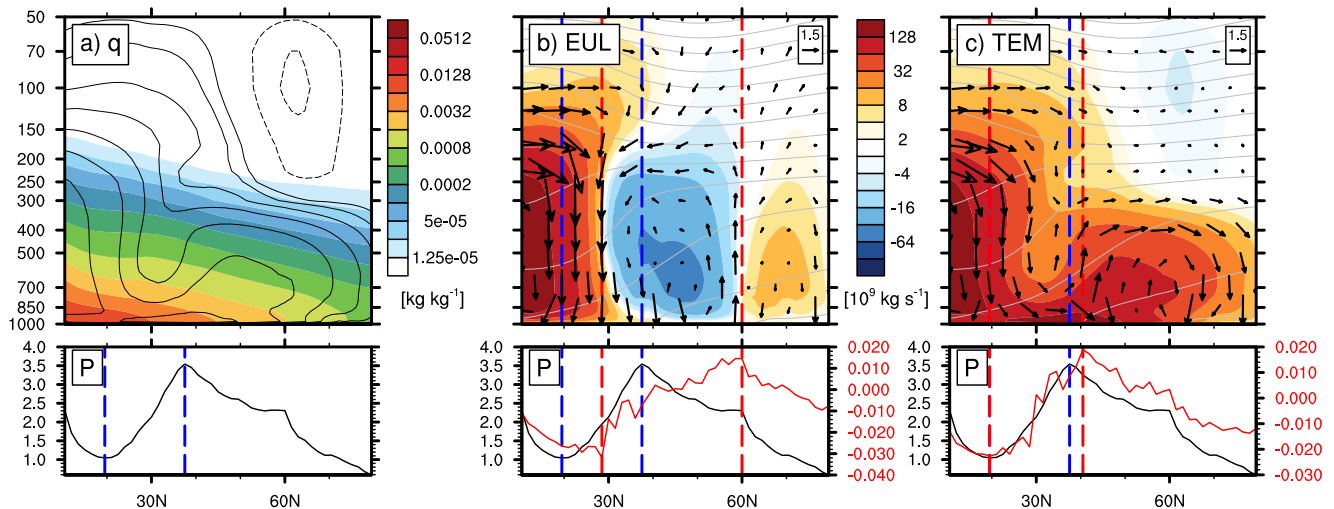


Fig. 1 Precipitation distribution and the Eulerian vs TEM vertical motion. DJF climatology (shading) is shown for **a** zonal mean specific humidity, **b** the conventional Eulerian mean mass streamfunction (and the Eulerian mean wind vectors), and **c** the TEM mass streamfunction (and the TEM wind vectors), along with corresponding zonal mean precipitation and vertical wind (black and colored lines, respectively, in the bottom panels). The TEM mass streamfunction is repeated in **a** (contour). Note that the shading levels for the streamfunction and specific humidity are unevenly distributed, as shown in the label bar. We use the same shading levels for Figs. 1b, c. The units for precipitation are mm day^{-1} . The dashed blue lines in the bottom panels indicate the subtropical minimum and midlatitude maximum of precipitation. The dashed red lines indicate the positive and negative maxima of $\bar{\omega}_{500}$ ($\bar{\omega}_{500}^*$), the pressure velocity of the conventional Eulerian (TEM) mean at 500 hPa.

eddy fluxes will also account for the latitudinal location of the precipitation maximum/minimum.

In synoptic meteorology, it is well known that cold season midlatitude precipitation is often associated with the warm conveyor belts (WCBs) of typical extratropical cyclone (EC, hereafter) systems. WCBs are characterized by the rapid rising of moist air, generally in the poleward direction in the warm sectors of EC systems^{10–12}. From this perspective, the coincidence of the midlatitude precipitation maximum and the rising branch of the dip is interesting, raising the question of whether the rising branch of the dip (Fig. 1c) could be a zonal mean expression of WCBs. In the same vein, the descending branch of the dip may be an expression of the zonal mean of dry intrusions (Dis) of EC systems. Raveh-Rubin¹³ showed that the descent of dry air from the upper troposphere/lower stratosphere down to the boundary layer promotes evaporation, thereby supplying moisture for WCBs in the same storm systems.

Synthesizing this line of evidence from existing theories, observations, and our analysis (Figs. 1 and 2) we hypothesize that if the EMF were sufficiently stronger than its climatology the rising branch of the dip and the precipitation peak would occur at 60°N, hence that the EMF plays a pivotal role in determining latitudinal distribution of extratropical precipitation. The goal of the rest of our analyses is to test this hypothesis using observation-based data. Our approach is to identify days when the instantaneous EMF projects positively or negatively onto its climatology and contrast the associated TEM circulation and precipitation anomalies with their respective climatology. Although daily time-scale process cannot fully capture all relevant processes for the climatology, such as the feedback by surface friction, our analyses with daily data can reveal the transient evolution from the occurrence of EMF anomalies to the TEM circulation and precipitation anomalies. The surface friction feedback does not change the physical picture under consideration because surface friction reinforces the EMF-driven overturning circulation¹⁴. If the hypothesis is correct, for positive EMF projections, we expect to see a poleward shift of the maximum upward TEM motion, producing broader dip, as well as a poleward displacement of the precipitation maximum. As we will see, if the

same exercise is applied to the EHF, the resulting change in the precipitation distribution is far less dramatic. Although it is beyond the scope of this study to demonstrate that the TEM dip is a zonal mean expression of the well-known synoptic features of Dis and WCBs, we present some evidence supporting this possibility in the hope of motivating more comprehensive analyses in the future.

RESULTS

Role of broad vs. narrow dip structure in precipitation

To examine the role of the climatological EMF in the TEM dip formation and midlatitude precipitation maximum, we construct an index by projecting the daily EMF over the midlatitude band of 35°N–55°N onto its DJF climatology (Materials and Methods). Because the climatological EMF converges in midlatitudes, this index measures the strength of a given day's midlatitude EMF convergence. At lag day 0 of the positive phase, anomalously poleward EMF results in an EP flux divergence/convergence pair in the upper troposphere, centered near 50°N and 30°N, respectively (Fig. 3a). In contrast, at lag day 0 of the negative phase, anomalously equatorward EMF can be seen, along with the EP flux divergence/convergence anomalies of the reversed sign (Fig. 3b). The EMF fluctuation has a lifespan of about seven days (Supplementary Fig. 1), which is consistent with the time scale of the lifecycle of a typical baroclinic disturbance¹⁵. Consistent with our hypothesis, the positive (negative) phase produces a broad (narrow) dip (Fig. 4). Henceforth, we refer to the positive (negative) phase as broad (narrow) dip case.

For the broad dip case, the corresponding TEM circulation anomaly displays a clockwise (counter-clockwise) overturning circulation anomaly in the tropics (midlatitudes) (Fig. 3c). For the narrow dip case, the TEM streamfunction anomalies show the opposite sign (Fig. 3d). Although the index is based on EMF, the EP flux divergence/convergence anomalies considered here also show contributions from the anomalous vertical EP flux vectors (Supplementary Fig. 2). However, it is the vertical integral of the EP flux divergence that influences the TEM streamfunction (Eqs. 2 and 5), and when vertically integrated from 100 hPa through to 850 hPa, the EMF is the primary driver of the TEM anomalies

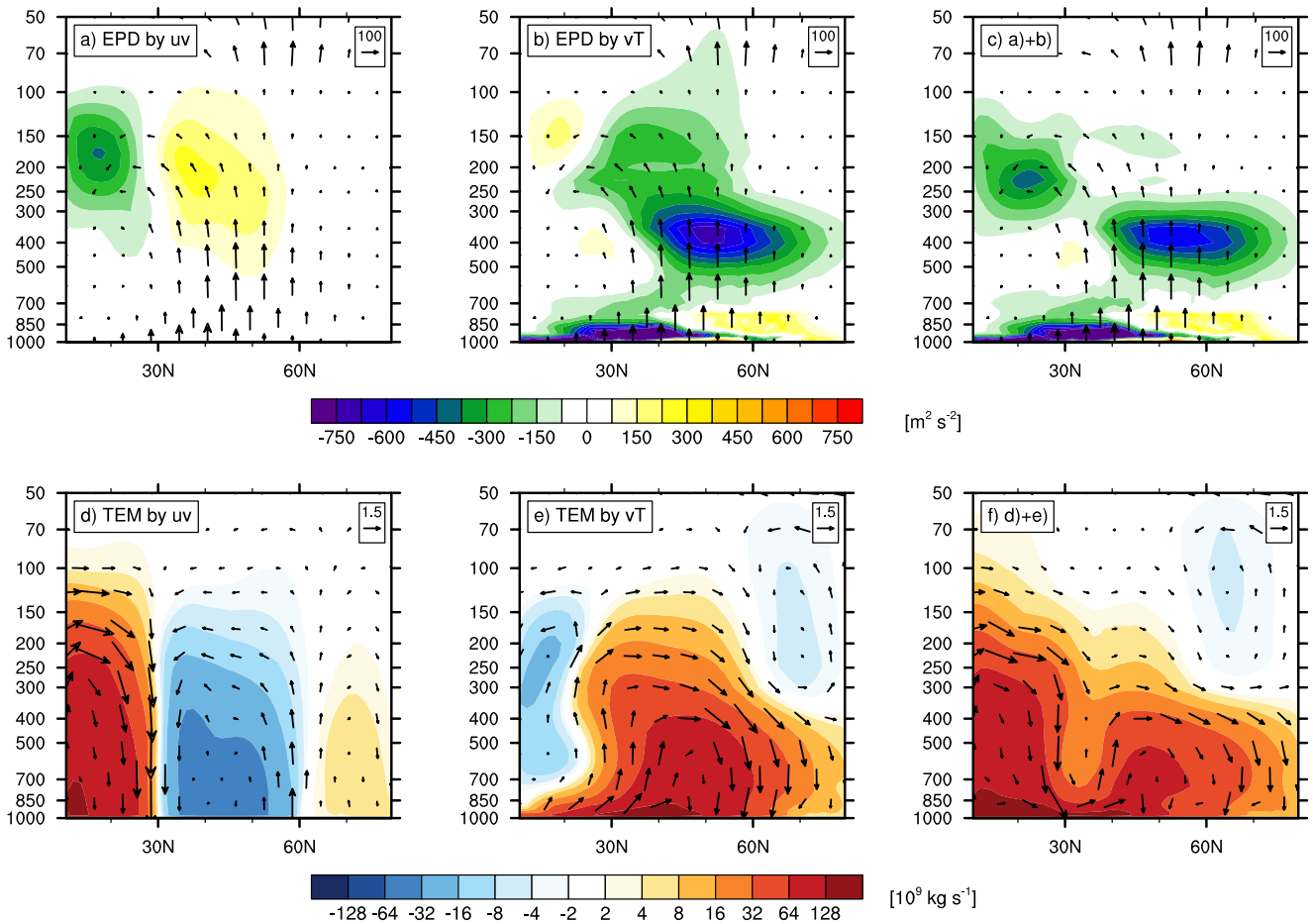


Fig. 2 Eddy heat and momentum flux contributions to the TEM circulation. DJF climatology (shading) is shown for (top panels) EP flux divergence and (bottom panels) TEM streamfunction (and the TEM wind vectors), which are driven by the (a, d) EMF, (b, e) eddy heat flux, and (c, f) both EMF and eddy heat flux. The total EP flux vectors are also shown in a–c. The TEM streamfunction by the EMF is obtained by the balance $\bar{v}^* = -\frac{1}{f a \cos \phi} \nabla \cdot \mathbf{F}$ for an inviscid and steady assumption. The eddy heat flux driven TEM streamfunction is obtained by setting $\bar{v}^* = -\left(\frac{v\theta'}{\theta_p}\right)_p$. The shading interval for the EP flux divergence is $75 \text{ m}^2 \text{ s}^{-2}$, as indicated by the label bar. As in Fig. 1, uneven shading levels are chosen for the streamfunction. The reference vector magnitudes are shown in the upper right of each panel.

(Supplementary Fig. 3). The result of Supplementary Fig. 3 remains robust when the vertical integral is performed for 100–500 hPa (now shown). Moreover, the midlatitude EHF index, measured by projecting the daily EHF onto its DJF climatology (Materials and Methods), is near zero at lag day 0 of the EMF events (dashed lines in Supplementary Fig. 1), suggesting that its overall contribution is small.

Composites of total TEM circulation show a remarkable change of the dip structure in response to the anomalous EMF (Fig. 4a, b). The total field is the sum of the TEM streamfunction climatology (Fig. 1c) and the TEM anomalies for the corresponding phases (Fig. 3c, d). During the broad dip case, the dip is substantially broadened, extending over approximately 20°N – 52°N , reaching its deepest extent in the lower troposphere near 50°N (shading in Fig. 4a). In contrast, during the narrow dip case, the dip is displaced equatorward to approximately 30°N and deepened, and its meridional width narrows (shading in Fig. 4b). The narrow dip case exhibits descending and ascending motions between 15°N – 25°N and 35°N – 45°N , respectively.

Consistent with the changes in the TEM overturning circulation, midlatitude precipitation shows a striking dependence on the EMF as well (Fig. 4c, d). For both the convective and large-scale precipitation anomalies, we find an increase (decrease) in

precipitation (dashed lines in Fig. 4c, d) over the region of upward (downward) TEM circulation anomalies (Fig. 3c, d). As for the TEM streamfunction anomalies, the precipitation anomalies show similar patterns with reversed signs between the broad and narrow dip cases. The differences between the broad and narrow dip precipitation anomalies are substantial, ranging between -0.3 – 0.3 mm day^{-1} for anomalies with a two standard deviation amplitude—comprising as large as 30%–50% of the climatological precipitation depending on the phase and latitude (Supplementary Fig. 4a). The fraction is still substantial ($\sim 20\%$ – 30% near 30°N and 60°N) when one standard deviation is used to define the phases (Supplementary Fig. 4b). Overall, the large-scale condensation component makes a more substantial contribution than the convective component (blue and red dashed lines in Fig. 4c, d), even though the two types of precipitation show anomalies of the same sign. As a result, for the broad dip case, precipitation anomalies generate extensive total precipitation over the entire midlatitudes, evidenced by the two maxima near 35°N and 60°N (solid lines in Fig. 4c); meanwhile, for the narrow dip case, one sharp peak can be seen in total precipitation over 35°N – 40°N (solid lines in Fig. 4d). Such strong changes in the global hydrological cycle associated with the EMF have not been reported despite connections between eddy-

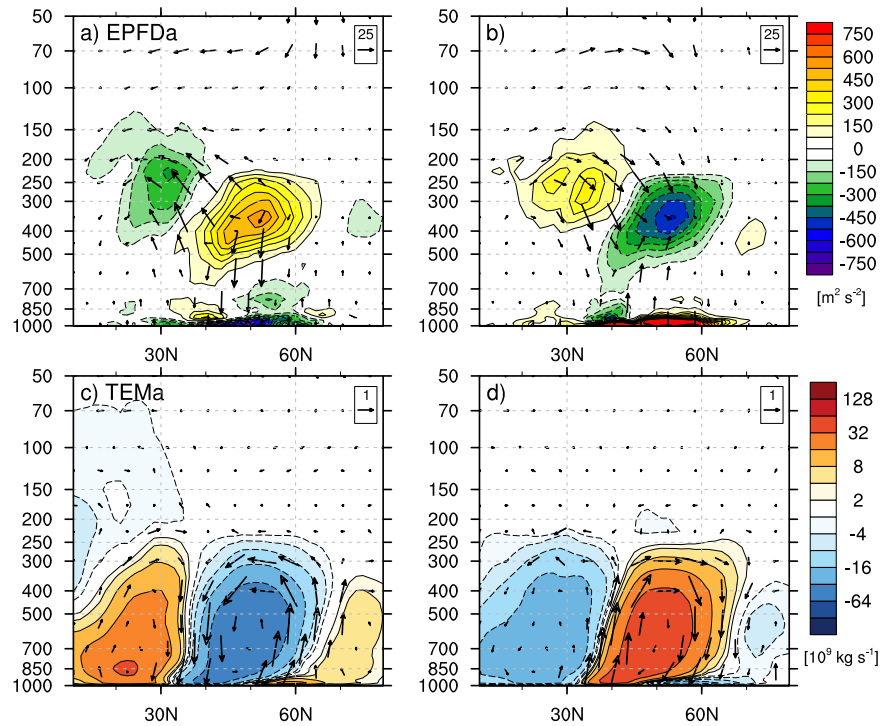


Fig. 3 EP flux and TEM circulation anomalies. Composites of the anomalous EP flux vectors and the EP flux divergence (shading) are shown for the **a** broad dip and **b** narrow dip cases, defined based on the two standard deviation threshold values of the midlatitude EMF index. **c, d** Show composites of the TEM mass streamfunction anomalies. As in Fig. 1, uneven shading levels are chosen for the streamfunction. The reference vector magnitude is shown in the upper right of each panel.

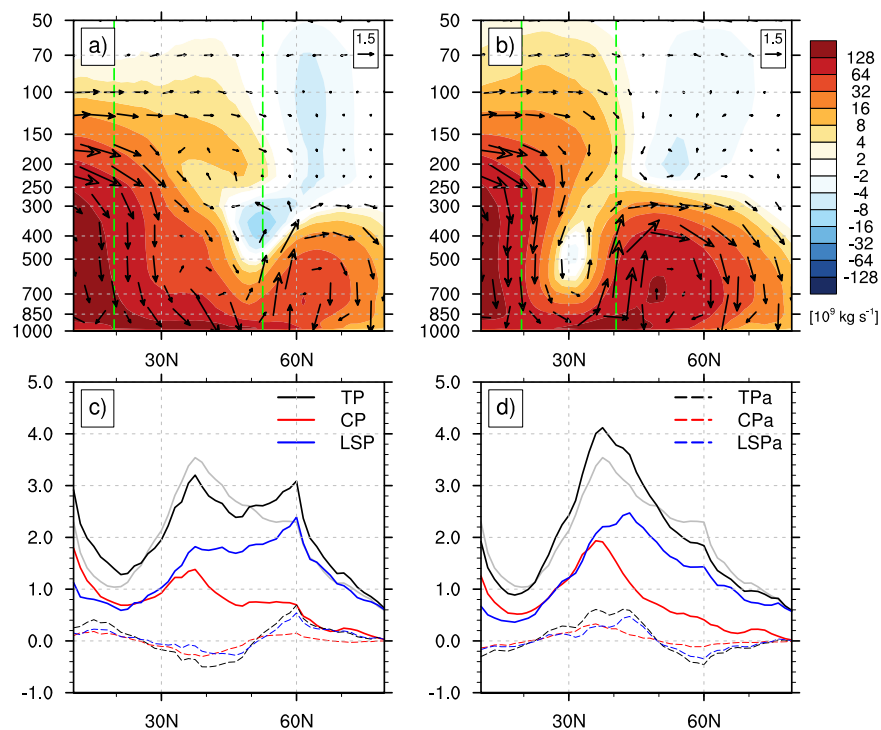


Fig. 4 TEM circulation and precipitation distribution. Composites of the TEM mass streamfunction are shown for the **a** broad dip and **b** narrow dip cases, defined based on the two standard deviation threshold value of the EMF index. As in Fig. 1, uneven shading levels are chosen for the streamfunction. **c, d** Show the corresponding zonal mean (solid black) total, (solid red) convective, (solid blue) and large-scale precipitation, along with (dashed lines) their anomalies. The climatology of total precipitation is shown in solid gray. The units for precipitation are mm day^{-1} .

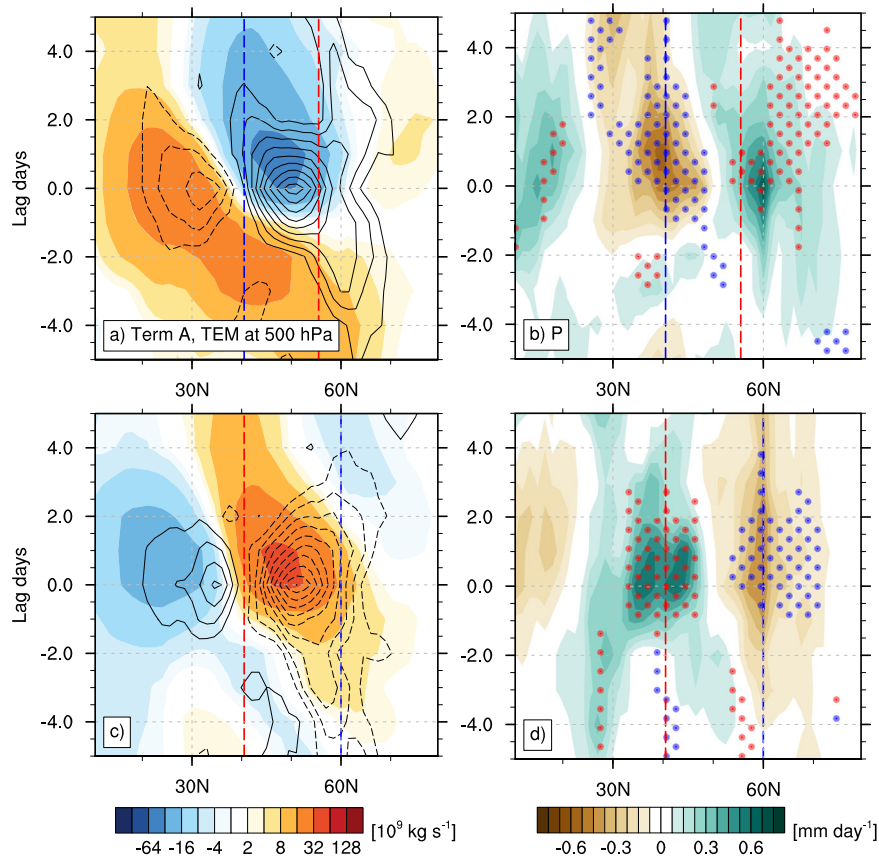


Fig. 5 Evolution of EMF, TEM circulation, and precipitation. Lagged composites are performed for (top panels) broad dip and (bottom panels) narrow dip cases. **a, c** Show Term A (contours) in Eq. (11), along with the TEM mass streamfunction anomalies (shading), averaged between 300–1000 hPa. The contour interval for Term A is $10^8 \text{ m}^2 \text{ kg}^{-1} \text{ s}^{-1}$, and as in Fig. 1, uneven shading levels are chosen for the streamfunction. **b, d** Present anomalies of zonal mean total precipitation. Also, the latitudes of vertical pressure velocity exceeding $2.5 \times 10^{-3} \text{ Pa s}^{-1}$ are indicated by blue dots, while the latitudes of less than $-2.5 \times 10^{-3} \text{ Pa s}^{-1}$ vertical velocity are indicated by red dots.

driven jet and precipitation¹⁶. The results remain robust when subsampled by the strength of the EHF (Supplementary Figs. 5–6), indicating that the EHF does not play an important role in the EMF-based precipitation composites.

Repeating the analysis for anomalous EHF events, we find that precipitation anomalies constitute approximately one half of those associated with the EMF (Supplementary Figs. 4c, d). Here, the anomalous EHF events are defined when the EHF index exceeds its two standard deviations (Materials and Methods). This result indicates that EMF-related precipitation anomalies are not a result of the EMF being merely associated with the EHF, and instead that the EMF plays the dominant role in regulating the precipitation distribution.

The EMF also noticeably alters the strength and location of the subtropical precipitation minimums. Ascending (descending) anomalies between 10°N – 20°N (20°N – 30°N) in the broad dip case coincide with positive (negative) precipitation anomalies (dashed lines in Fig. 4c) in the region, and a similar pattern with the opposite signs occurs for the narrow dip case (dashed lines in Fig. 4d). The total precipitation minimum shifts poleward to approximately 25°N in the broad dip case (Fig. 4c), while it shifts equatorward to 15°N in narrow dip case (Fig. 4d). Because of the low climatological precipitation, the fractions of precipitation changes in the subtropics can be as large as 20%–50%—comparable to those that occur in midlatitudes (Supplementary Fig. 4a).

The temporal evolution of the EMF, TEM, and precipitation anomalies partially support the EMF \rightarrow TEM and precipitation anomalies causal relationship that we describe here using physical

reasoning. Lagged composites for the anomalous EMF events reveal that the EMF forcing in the residual circulation equation (term A in Eq. 11) indeed generates the changes in the TEM overturning circulation and precipitation (Fig. 5). By construction, term A of Eq. (11) peaks at lag day 0 in both phases (contours in Fig. 5a, b). Because of the elliptic operator on the left-hand side of Eq. (11), positive values for term A should lead to a negative TEM streamfunction anomaly and vice versa for negative term A values. In fact, we observe such a relationship near lag day 0 in the subtropics and in the midlatitudes, with the momentum forcing (term A) being lagged 1–2 days by the streamfunction (shading in Fig. 5a, b). Precipitation anomalies are also maximized about 1–2 days after the peak momentum forcing (shading in Fig. 5c, d). Enhanced (reduced) precipitation coincides with anomalous ascent (descent) in the TEM circulation (dots in Fig. 5c, d). The concurrent timing of the TEM and precipitation anomalies suggests that not only precipitation responds to the TEM rising motion, but also latent heating associated with the precipitation might further enhance the rising motion.

The time lag between the EMF, the TEM circulation, and precipitation is consistent with the finding in synoptics studies that Rossby wave breaking is accompanied by precipitation anomalies through changes in the WCB^{17–19}. The high moisture content associated with the WCB is fed by a low-level air stream^{20,21} that was recently termed as a feeder airstream (FA)¹⁰. The FA in turn is attributed to a DI that moisturizes the FA through evaporation¹³. Because DIs originate in the upper troposphere/lower stratosphere where potential vorticity (PV) is higher than in the mid- and lower troposphere^{22–24}, and because the TEM

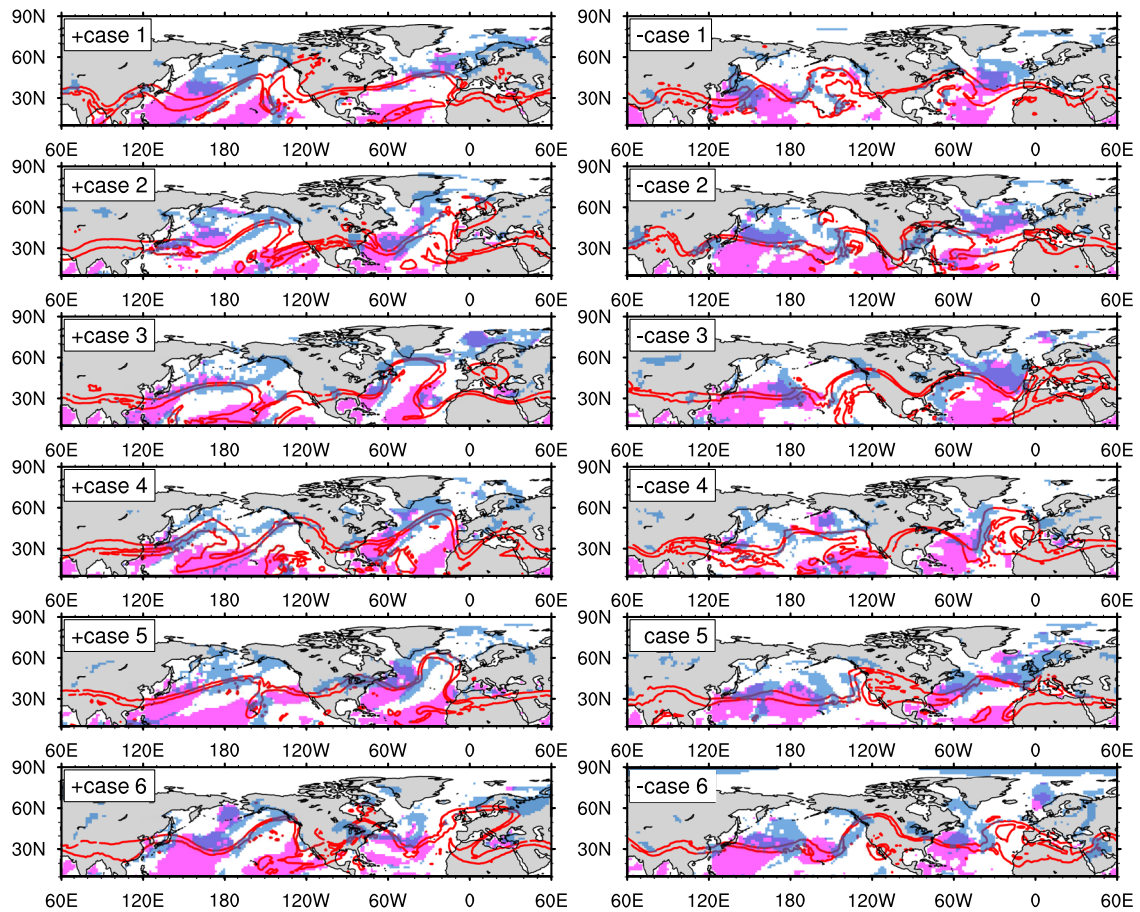


Fig. 6 Horizontal structure of PV, evaporation and precipitation during selected EMF events. Daily snapshots are shown for lag day 0 of the six selected anomalous EMF events for the (left) broad dip and (right) narrow dip cases. The six events are arbitrarily sampled out of the days that exceed the 2.4 standard deviation threshold value and are listed in Supplementary Table 1. Regions with evaporation rates greater than 5 mm day^{-1} (magenta shading) are shown, with positive values being set to indicate an upward evaporative flux. Also, regions with total precipitation greater than 2 mm day^{-1} (blue shading) are also shown. The 5 and 2 mm day^{-1} thresholds are subjectively selected to display the location and curvature of the evaporation and precipitation, respectively. The 0.5- and 2-PVU isolines on the 325-K isentropic surface (red lines) are shown to indicate the mixing region of stratospheric and tropospheric air masses.

circulation is a reasonable approximation of Lagrangian motion^{25–27}, the PV transport via the TEM residual circulation will be used as a proxy for the DI (Figs. 7a, b). Similarly, the moisture transport associated with WCB can be represented by the moisture transport of the residual circulation (Figs. 7e, f). We will also show that the EMF forcing is accompanied by changes in evaporation (Figs. 7c, d) and that the evaporation is enhanced where the near-surface convergence of PV transport by the residual wind is anomalously positive (below 850 hPa); although these positive anomalies are rather marginal, they occur where the upper troposphere/lower stratosphere air descends, as indicated by the TEM circulation pattern.

DI, FA, and WCB-like features in TEM dip structure

To examine the synoptic features that are smoothed out in our zonal mean composites, daily snapshots of some selected EMF events are shown in Fig. 6. We use the 2.4 standard deviation threshold value for the date selections (see Materials and Methods and Supplementary Table 1) to highlight the difference between the two dip cases. In the broad dip cases, which are subsamples of broad dip composite members, we find strong equatorward intrusions of dry, high PV air, as well as poleward intrusions of moist, low PV air, as indicated by the large meridional displacements of the 0.5- and 2-PVU lines on the 325-K isentropic surface

(red lines in the left panels). The two PVU lines are chosen to show the meridional and vertical displacements of moist tropospheric (less than ~ 1 PVU) and dry stratospheric air (greater than 2 PVU)^{28,29}. The equatorward high PV intrusions are consistent with the picture of a DI that starts in the high latitude stratosphere and then quickly shifts to the subtropics in the troposphere. In addition, the PV intrusions are particularly noticeable over the ocean in the selected cases, which is consistent with climatological frequency of Dis being more pronounced over the ocean than land^{13,19,30}. In the narrow dip cases, the 0.5- and 2-PVU lines give visual impression of not being as wavy as those in the broad dip cases, suggesting that the meridional PV intrusions are relatively modest (red lines in the right panels). Although the waviness is not quantified, it is generally consistent with the enhanced climatological equatorward wave activity during the positive phase (e.g., Fig. 3).

The daily snapshots also provide some evidence that the EMF contributes to the precipitation anomalies through changes in evaporation and, subsequently, WCB-like moisture transport. Figure 6 shows that the evaporation rates (magenta shading) vary significantly in strength along the 0.5- and 2-PVU lines, particularly over the ocean, while precipitation rates (blue shading) tend to be enhanced slightly downstream of the evaporation. Evaporation is generally substantial when dry, high PV air is displaced equatorward and downward and vice versa for

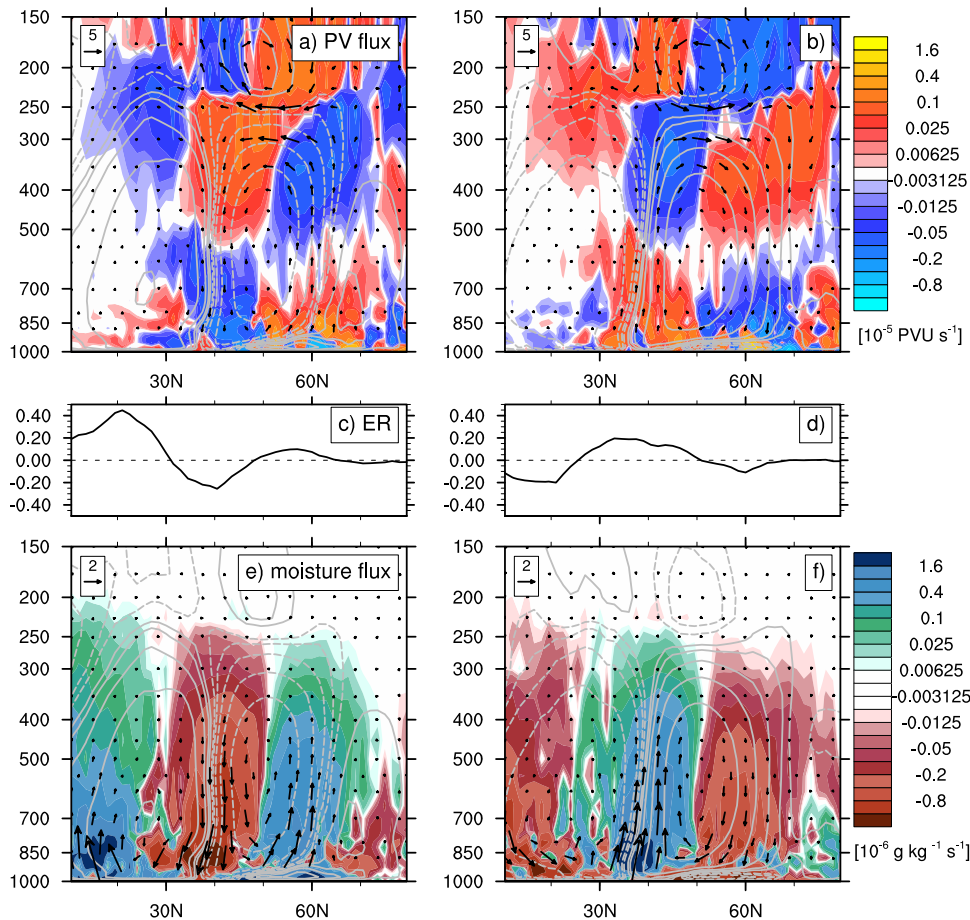


Fig. 7 Relationship between surface evaporation and high PV air transported by the TEM circulation. Composites are presented for the (left panels) broad dip and (right panels) narrow dip cases as in Fig. 4, except that (a, b) show the residual PV flux anomalies (vectors), (c, d) the evaporation rate anomalies, and (e, f) the residual moisture flux anomalies (vectors). Here the residual fluxes are computed using the residual wind to represent the transport by the Eulerian mean and the advective effect of the eddies (Materials and Methods). Shading corresponds to the PV flux convergence and moisture flux convergence anomalies (with uneven intervals), as indicated by the label bars. The evaporation rate units are mm day^{-1} . The TEM streamfunction anomaly composites are superimposed by contours in the panels (a, b, e, f).

the poleward and upward displacement of moist air. For example, in broad dip case 1, strong evaporation near 20°N , 150°W is collocated with high PV intrusion, while moist air intruded to 50°N , 160°W is accompanied by weak evaporation. In the narrow dip cases, we observe similar features, such as enhanced evaporation near 30°N , 150°W of narrow dip case 6. Also, evaporation rates are very weak at the poleward edges of moist air intrusions, e.g., at 50°N , 140°W of positive case 2 or at 50°N , 110°W of narrow dip case 3. Interestingly, within wave segments bounded by two PV crests, precipitation tends to be strong downstream of the enhanced evaporation. This suggests that the evaporated moisture may get advected before being precipitated out. However, the EMF-evaporation-precipitation mechanism requires a very efficient transport of moisture along a preferred path, and our analyses do not rule out alternate explanations for the spatial coincidence between evaporation and precipitation anomalies, such as the dry air inducing a lower-level jet along the preferred path of moisture transport. In fact, the precipitation structure closely aligns with vertically integrated water vapor transport (Supplementary Fig. 7), indicating the importance of atmospheric moisture transport. Evaporation can be scaled by the surface wind speed, instead of by the dryness of the air, but our calculation shows that the evaporation-wind speed relationship does not hold up in every case (not shown), indicating that dryness also plays an important role.

Returning to the composites, we find consistent features in the PV anomalies on the 325-K isentropic surface, upward evaporation rate anomalies, and precipitation rate anomalies (Supplementary Fig. 8). Consistent with the visual impressions given by the daily snapshots, the precipitation anomalies occur slightly downstream of the evaporation anomalies, e.g., reduced precipitation and evaporation near 45°N , 150°W and 40°N , 140°W , respectively, for the broad dip case and enhanced precipitation and evaporation near 35°N , 160°W and 35°N , 180° , respectively, for the narrow dip case (the middle and bottom panels). Also, evaporation enhancement occurs in areas of dry stratospheric air intrusion, represented by increased PV on the 325-K surface, while reduced evaporation coincides with reduced PV (the top and middle panels). However, because of the compositing, the differences in the meridional fluctuations between the two cases are averaged out.

We examine the residual moisture ($\overline{v^*q}$) and PV fluxes ($\overline{v^*\overline{\Pi}}$; Materials and Methods) as a proxy for zonal mean tracer transport. The residual fluxes represent the transport by the Eulerian mean and the advective effect of the eddies and exclude the diffusive effect of the eddies³. Although they are not direct measures of Dis and WCBs, these residual fluxes provide some evidence of how the EMF and hence the midlatitude dip alters zonal mean precipitation via dry and moist air transport. As shown in Fig. 7, we observe features consistent with the anatomy of extratropical cyclones: latitudinal alignment of enhanced evaporation,

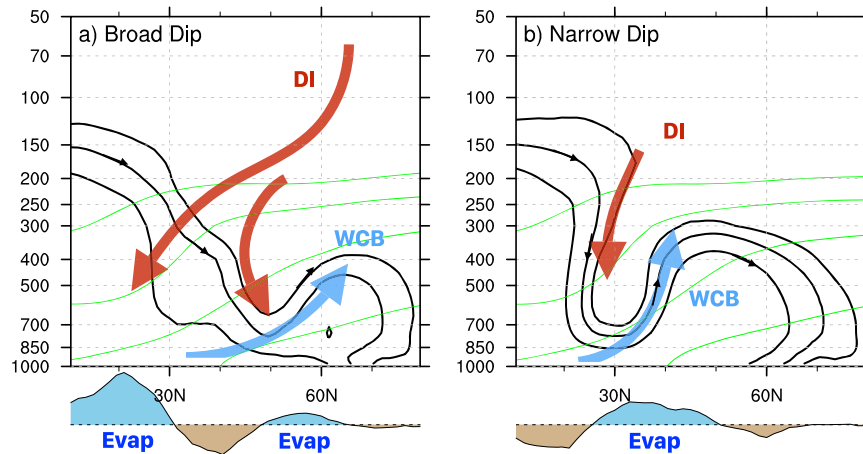


Fig. 8 Hypothesized relationship between the TEM vertical motion, DI, and WCB. Schematics of the TEM mass streamfunction (contours) and accompanying DI-like dry air intrusion (red arrows), evaporation (the line plot in the bottom), and WCB-like moisture transport (blue arrows) are shown for the **a** broad dip and **b** narrow dip cases. The blue (brown) shading in the line plot indicates enhanced (reduced) upward evaporation rates compared to the cold season climatology. The black arrows indicate the direction of the TEM overturning circulation. The green lines show zonal mean isentropic surfaces.

anomalously positive residual PV flux convergence, and residual moisture flux convergence. In particular, we observe enhanced (reduced) poleward moisture transport in the lower midlatitude troposphere (30°N–60°N) during the broad (narrow) dip cases (vectors in Fig. 7e, f). The anomalous residual moisture flux vectors result in the anomalous convergence of moist air in the subpolar (subtropical) region during broad (narrow) dip cases (shading in Fig. 7e, f), which coincides with the anomalous precipitation (Fig. 4). Evaporation is also enhanced over the region of anomalous moisture flux convergence and precipitation (Fig. 7c, d), as shown in Fig. 6 and S9. This indicates that the air moistened by evaporation gets advected downstream and forms precipitation (Fig. 6). We find an excellent match between enhanced (reduced) evaporation and near-surface anomalous residual PV flux convergence (divergence) (shading in Fig. 7a, b), consistent with the results shown in Fig. 6 and Supplementary Fig. 8.

DISCUSSION

The transformed Eulerian mean (TEM) overturning circulation exhibits a U-shaped dip structure in midlatitudes. The dip is primarily driven by eddy momentum fluxes (EMFs) and eddy heat fluxes (EHFs), while diabatic heating is expected to play an important role for the subtropical branch of the dip. We have shown that the EMF-driven TEM circulation can substantially reshape the zonal mean distribution of cold season precipitation. When an anomalously poleward EMF broadens the dip, the total precipitation is distributed relatively evenly between 30°N–60°N (Fig. 4c). In contrast, total precipitation peaks more sharply than the climatology between 30°N–40°N when the dip is limited to the subtropics due to anomalously equatorward EMF (Fig. 4d).

Based on our findings, we suggest that the sinking branch of the TEM circulation corresponds to a zonal mean expression of dry intrusions (DIs) and the rising branch to a zonal mean expression of warm conveyor belts (WCBs) of typical extratropical cyclones. This process is summarized in the schematic diagram shown in Fig. 8. In the broad dip case (Fig. 8a), near 20°N and 55°N where the descending motion is anomalously strong, we suggest that DI occurrence (red arrows) is enhanced as evidenced by the convergence of PV by the residual wind; subsequently evaporation increases (shading) and WCBs (as evidenced by the moisture flux) extend to the subpolar region.

During the narrow dip case, these features tend to congregate in the subtropics (Fig. 8b). However, an examination of the statistics of these synoptic precipitation system trajectories is not performed in the present study. Further investigation is needed to establish a more precise connection between the zonal mean TEM perspective and the synoptic description.

We have emphasized that the EMF is the primary driver of the TEM anomaly during anomalous EMF events. This is because it is the vertical integral of the eddy forcing which results in TEM anomaly. However, in the baroclinic lifecycle paradigm, the EMF occurs during the barotropic decay phase that follows the baroclinic growth of enhanced EHF. Consistent with this picture, Supplementary Fig. 1 shows that EHF leads EMF by 2 days. However, further examination is required to fully understand the role of EHF in the TEM and precipitation during the EMF events because anomalous EMF can take place for example in response to tropical convective forcing^{31,32}.

Our findings highlight the importance of the strength and direction of the EMF in zonal mean precipitation distributions. This result suggests that precipitation amount and distribution can be highly sensitive to the potential vorticity gradient and shear of the background flow because they play an important role determining the direction of the EMF^{4,33}. It is therefore plausible that changes in upper tropospheric/lower stratospheric wind can have an important impact on the future states of precipitation distributions. Nevertheless, this potentially critical aspect of climate change is relatively poorly understood³⁴. Given the importance of water in the warming climate, our findings underscore the need for a better understanding of these dynamic changes.

METHODS

Observational data

We use the fifth generation of the atmospheric reanalysis product of the European Centre for Medium-Range Weather Forecasts (ERA5)³⁵ to examine the past 41 Northern Hemisphere winters (December–February (DJF)) from 1979/80 to 2019/20. The dataset was originally downloaded from the Copernicus Climate Change Service website (<https://cds.climate.copernicus.eu/>) for every 6 h from 00 UTC to 18 UTC with horizontal resolution of 0.25° latitude × 0.25° longitude before we applied the daily mean and bilinear interpolation to the 1.5° latitude × 1.5° longitude grid.

TEM mass streamfunction and TEM equations

To examine the zonal mean overturning circulation, we define the zonal mean mass streamfunction, $\bar{\psi}$, as:

$$\bar{\psi}(t, \phi, p) = \frac{2\pi a \cos(\phi)}{g} \int_p^0 \bar{v}(t, \phi, p) dp, \quad (1)$$

where a is the radius of the Earth, g gravity, P_s surface pressure, and v meridional wind. Here, the overbar indicates the zonal mean, and $\bar{\psi}$ is a function of time (t), latitude (ϕ), and pressure (p).

The TEM mass streamfunction, $\bar{\psi}^*$, is similarly defined as:

$$\bar{\psi}^*(t, \phi, p) = \frac{2\pi a \cos(\phi)}{g} \int_p^0 \bar{v}^*(t, \phi, p) dp. \quad (2)$$

Here, the residual mean meridional velocity \bar{v}^* is defined as:

$$\bar{v}^* = \bar{v} - \left(\frac{v'\theta'}{\bar{\theta}_p} \right)_p, \quad (3)$$

where θ is potential temperature, and the prime denotes the deviation from the zonal mean. Likewise, the residual mean vertical velocity \bar{w}^* is defined as:

$$\bar{w}^* = \bar{w} + \left(\frac{1}{a \cos \phi} \right) \left(\frac{v'\theta' \cos \phi}{\bar{\theta}_p} \right)_\phi. \quad (4)$$

By rearranging the eddy heat flux contributions³⁶, the following quasigeostrophic (QG) TEM momentum, thermodynamic energy, and continuity equations can be obtained:

$$\frac{\partial \bar{u}}{\partial t} - f \bar{v}^* = \frac{1}{a \cos \phi} \nabla \cdot \mathbf{F} + \bar{X}, \quad (5)$$

$$\frac{\partial \bar{\theta}}{\partial t} + \bar{\theta}_p \bar{w}^* = \bar{Q}, \quad (6)$$

$$\frac{1}{a \cos \phi} \frac{\partial(\bar{v}^* \cos \phi)}{\partial \phi} + \frac{\partial \bar{w}^*}{\partial p} = 0. \quad (7)$$

where u is the zonal wind, f is the Coriolis parameter, \bar{X} is the zonal mean frictional forcing, and \bar{Q} is the zonal mean diabatic forcing. The meridional and vertical EP flux vectors (\mathbf{F}) in the QG approximation can be given respectively as:

$$F^\phi = -a \cos \phi \overline{u'v'}, \quad (8)$$

$$F^p = a \cos \phi f \frac{\overline{v'\theta'}}{\bar{\theta}_p}. \quad (9)$$

Through thermal wind balance, Eqs. (5–6) can be combined as:

$$\frac{f^2 g}{2\pi a \cos \phi} \frac{\partial^2}{\partial p^2} \bar{\psi}^* + \frac{Rg}{2\pi a^2 \cos \phi} \frac{\partial}{\partial \phi} \left(\bar{\theta}_p \frac{\partial}{\partial \phi} \bar{\psi}^* \right) = f \frac{\partial}{\partial p} \left(\frac{1}{a \cos \phi} \nabla \cdot \mathbf{F} \right) + f \frac{\partial}{\partial p} \left(\bar{X} \right) - \frac{\partial}{\partial \phi} \left(\bar{Q} \right), \quad (10)$$

where

$$f \frac{\partial}{\partial p} \left(\frac{1}{a \cos \phi} \nabla \cdot \mathbf{F} \right) = \underbrace{f \frac{\partial}{\partial p} \left(\frac{1}{a^2 \cos^2 \phi} \frac{\partial F^\phi \cos \phi}{\partial \phi} \right)}_A + \underbrace{f \frac{\partial^2}{\partial p^2} (F^p)}_B. \quad (11)$$

We compute the residual moisture ($\bar{v}^* \bar{q}$) and PV fluxes ($\bar{v}^* \bar{\Pi}$) using the residual mean meridional velocity \bar{v}^* , zonal mean specific humidity (\bar{q}), and the zonal mean Ertel's PV ($\bar{\Pi}$).

In a steady, inviscid flow, the residual meridional wind (\bar{v}^*) can be obtained through the balance between the Coriolis torque

($f\bar{v}^*$) and the EP flux divergence ($\frac{1}{a \cos \phi} \nabla \cdot \mathbf{F}$). Using (5), the corresponding $\bar{\psi}^*(t, \phi, p)$ can then be computed. This procedure was used to construct Figs. 2d, e which, respectively, show the individual contributions by F^ϕ and F^p .

Definition of Eddy Flux index

We construct an eddy momentum flux (EMF) index (I_M) by measuring the similarity between the climatological DJF EMF and the daily EMF ($u'v'$) over the midlatitudes. The similarity between these two EMFs is determined by projecting the daily flux onto the climatological flux with a cosine latitude factor as, i.e.,

$$I_M = \sum_{\phi, p} \overline{[u'v']^{DJF}} \overline{u'v' \cos(\phi)}, \quad (12)$$

where $\overline{[\]^{DJF}}$ indicates the time average over all DJF seasons. The projection is carried out for the domain between 35°N–55°N and 250–1000 hPa. We select this domain to capture the maximum of DJF EMF convergence between 40°N–50°N. However, some reasonable variations of the domain—e.g., between 30°N–45°N and 45°N–60°N—do not change the main results of this study. The index is standardized based on its mean and standard deviation.

Similarly, we compute an eddy heat flux (EHF) index (I_H) using the EHF ($v'\theta'$) as:

$$I_H = \sum_{\phi, p} \overline{[v'\theta']^{DJF}} \overline{v'\theta' \cos(\phi)}. \quad (13)$$

We again select the projection domain for the EHF to be between 35°N–55°N and 250–1000 hPa because its DJF climatology is centered near 45°N. The index is also standardized based on its mean and standard deviation.

In this study, we define the positive phase of an anomalous eddy flux event as taking place when the index is greater than two standard deviations. Similarly, we define the negative phase as occurring when the index is less than negative two standard deviations. This results in a sample of 93 (84) days for positive (negative) phase EMF events. For the EHF events, a sample of 86 (69) days are obtained its positive (negative) phase. We find that the main conclusions of the study remain robust when we use a one standard deviation threshold to define the phases.

DATA AVAILABILITY

ERA5 data are available from the Copernicus Climate Data Store, <https://cds.climate.copernicus.eu/>.

CODE AVAILABILITY

The codes used for analyses in this study are available on request from the authors.

Received: 29 July 2022; Accepted: 9 March 2023;

Published online: 25 March 2023

REFERENCES

- Catto, J. L., Jakob, C., Berry, G. & Nicholls, N. Relating global precipitation to atmospheric fronts. *Geophys. Res. Lett.* <https://doi.org/10.1029/2012GL051736> (2012).
- Hawcroft, M. K., Shaffrey, L. C., Hodges, K. I. & Dacre, H. F. How much Northern Hemisphere precipitation is associated with extratropical cyclones? *Geophys. Res. Lett.* <https://doi.org/10.1029/2012GL053866> (2012).
- Andrews, D. G., Holton, J. R. & Leovy, C. B. *Middle Atmosphere Dynamics*. Vol. 40 (Academic Press, 1987).

4. Andrews, D. G. & McIntyre, M. E. Planetary waves in horizontal and vertical shear: the generalized Eliassen-Palm relation and the mean zonal acceleration. *J. Atmos. Sci.* **33**, 2031–2048 (1976).
5. Held, I. M. & Schneider, T. The surface branch of the zonally averaged mass transport circulation in the troposphere. *J. Atmos. Sci.* **56**, 1688–1697 (1999).
6. Chen, G. The mean meridional circulation of the atmosphere using the mass above isentropes as the vertical coordinate. *J. Atmos. Sci.* **70**, 2197–2213 (2013).
7. Robinson, W. A. On the self-maintenance of midlatitude jets. *J. Atmos. Sci.* **63**, 2109–2122 (2006).
8. Haynes, P. H., McIntyre, M. E., Shepherd, T. G., Marks, C. J. & Shine, K. P. On the downward control of extratropical diabatic circulations by eddy-induced mean zonal forces. *J. Atmos. Sci.* **48**, 651–678 (1991).
9. Hoskins, B. J. & Yang, G. Y. The detailed dynamics of the Hadley cell. Part II: December–February. *J. Clim.* **34**, 805–823 (2021).
10. Dacre, H. F., Martínez-Alvarado, O. & Mbengue, C. O. Linking atmospheric rivers and warm conveyor Belt airflows. *J. Hydrometeorol.* **20**, 1183–1196 (2019).
11. Madonna, E., Wernli, H., Joos, H. & Martius, O. Warm conveyor belts in the ERA-Interim Dataset (1979–2010). Part I: climatology and potential vorticity evolution. *J. Clim.* **27**, 3–26 (2014).
12. Wernli, H. & Davies, H. C. A Lagrangian-based analysis of extratropical cyclones. I: the method and some applications. *Quart. J. Roy. Meteor. Soc.* **123**, 467–489 (1997).
13. Raveh-Rubin, S. Dry intrusions: Lagrangian climatology and dynamical impact on the planetary boundary layer. *J. Clim.* **30**, 6661–6682 (2017).
14. Kim, H.-k & Lee, S. Hadley cell dynamics in a primitive equation model. Part II: Nonaxisymmetric flow. *J. Atmos. Sci.* **58**, 2859–2871 (2001).
15. Simmons, A. J. & Hoskins, B. J. The life cycles of some nonlinear baroclinic waves. *J. Atmos. Sci.* **35**, 414–432 (1978).
16. Madonna, E., Li, C., Grams, C. M. & Woollings, T. The link between eddy-driven jet variability and weather regimes in the North Atlantic-European sector. *Quart. J. Roy. Meteor. Soc.* **143**, 2960–2972 (2017).
17. Catto, J. L. & Raveh-Rubin, S. Climatology and dynamics of the link between dry intrusions and cold fronts during winter. Part I: global climatology. *Clim. Dynam.* **53**, 1873–1892 (2019).
18. de Vries, A. J. A global climatological perspective on the importance of Rossby wave breaking and intense moisture transport for extreme precipitation events. *Weather Clim. Dynam.* **2**, 129–161 (2021).
19. Raveh-Rubin, S. & Catto, J. L. Climatology and dynamics of the link between dry intrusions and cold fronts during winter, Part II: Front-centred perspective. *Clim. Dynam.* **53**, 1893–1909 (2019).
20. Browning, K. A. & Roberts, N. M. Structure of a frontal cyclone. *Quart. J. Roy. Meteor. Soc.* **120**, 1535–1557 (1994).
21. Carlson, T. N. Airflow through midlatitude cyclones and the comma cloud pattern. *Mon. Wea. Rev.* **108**, 1498–1509 (1980).
22. Wernli, H. A Lagrangian-based analysis of extratropical cyclones. II: a detailed case-study. *Quart. J. Roy. Meteor. Soc.* **123**, 1677–1706 (1997).
23. Waugh, D. W. Impact of potential vorticity intrusions on subtropical upper tropospheric humidity. *J. Geophys. Res. Atmos.* <https://doi.org/10.1029/2004JD005664> (2005).
24. Browning, K. A. & Golding, B. W. Mesoscale aspects of a dry intrusion within a vigorous cyclone. *Quart. J. Roy. Meteor. Soc.* **121**, 463–493 (1995).
25. Dunkerton, T. On the mean meridional mass motions of the stratosphere and mesosphere. *J. Atmos. Sci.* **35**, 2325–2333 (1978).
26. Juckes, M. A generalization of the transformed Eulerian-mean meridional circulation. *Quart. J. Roy. Meteor. Soc.* **127**, 147–160 (2001).
27. Vallis, G. K. *Atmospheric and Oceanic Fluid Dynamics: Fundamentals and Large-scale Circulation* 2nd edn (Cambridge University Press, 2017).
28. Hoskins, B. J. Towards a PV- θ view of the general circulation. *Tellus A: Dyn. Meteorol. Oceanogr.* **43**, 27–36 (1991).
29. Hoskins, B. J., McIntyre, M. E. & Robertson, A. W. On the use and significance of isentropic potential vorticity maps. *Quart. J. Roy. Meteor. Soc.* **111**, 877–946 (1985).
30. Waugh, D. W. & Funatsu, B. M. Intrusions into the tropical upper troposphere: three-dimensional structure and accompanying ozone and OLR distributions. *J. Atmos. Sci.* **60**, 637–653 (2003).
31. Baggett, C. & Lee, S. Arctic warming induced by tropically forced tapping of available potential energy and the role of the planetary-scale waves. *J. Atmos. Sci.* **72**, 1562–1568 (2015).
32. Yoo, C., Lee, S. & Feldstein, S. B. Mechanisms of extratropical surface air temperature change in response to the Madden-Julian Oscillation. *J. Clim.* **25**, 5777–5790 (2012).
33. Held, I. M. Momentum transport by Quasi-geostrophic eddies. *J. Atmos. Sci.* **32**, 1494–1497 (1975).
34. Vallis, G. K., Zurita-Gotor, P., Cairns, C. & Kidston, J. Response of the large-scale structure of the atmosphere to global warming. *Quart. J. Roy. Meteor. Soc.* **141**, 1479–1501 (2015).
35. Hersbach, H. et al. The ERA5 global reanalysis. *Quart. J. Roy. Meteor. Soc.* **146**, 1999–2049 (2020).
36. Edmon, H. J., Hoskins, B. J. & McIntyre, M. E. Eliassen-palm cross sections for the troposphere. *J. Atmos. Sci.* **37**, 2600–2616 (1980).

ACKNOWLEDGEMENTS

C.Y. was supported by the National Research Foundation of Korea through grants NRF-2019R1C1C1003161 and by the Korea Environmental Industry and Technology Institute through grants KEITI-2022003560001. S.L. was supported by the National Science Foundation through grant AGS-1948667.

AUTHOR CONTRIBUTIONS

C.Y. and S.L. designed and performed research; C.Y. and S.L. wrote the paper.

COMPETING INTERESTS

The authors declare no competing interests.

ADDITIONAL INFORMATION

Supplementary information The online version contains supplementary material available at <https://doi.org/10.1038/s41612-023-00356-9>.

Correspondence and requests for materials should be addressed to Sukeyoung Lee.

Reprints and permission information is available at <http://www.nature.com/reprints>

Publisher's note Springer Nature remains neutral with regard to jurisdictional claims in published maps and institutional affiliations.



Open Access This article is licensed under a Creative Commons Attribution 4.0 International License, which permits use, sharing, adaptation, distribution and reproduction in any medium or format, as long as you give appropriate credit to the original author(s) and the source, provide a link to the Creative Commons license, and indicate if changes were made. The images or other third party material in this article are included in the article's Creative Commons license, unless indicated otherwise in a credit line to the material. If material is not included in the article's Creative Commons license and your intended use is not permitted by statutory regulation or exceeds the permitted use, you will need to obtain permission directly from the copyright holder. To view a copy of this license, visit <http://creativecommons.org/licenses/by/4.0/>.

© The Author(s) 2023